Influence of Mg on Solidification of Hypereutectic Cast Iron: X-ray Radiography Study

K. YAMANE, HIDEYUKI YASUDA, A. SUGIYAMA, T. NAGIRA, M. YOSHIYA, K. MORISHITA, K. UESUGI, A. TAKEUCHI, and Y. SUZUKI

Radiography using a synchrotron radiation X-ray source was performed to examine solidification and melting behaviors in hypereutectic cast iron specimens containing 0.002 and 0.05-mass pctMg. The solidification sequence in the alloy containing 0.002mass pctMg was (1) nucleation and growth of graphite particles of which transformed to a flake-like shape, (2) growth of γ-Fe dendrites, (3) nucleation of graphite particles ahead of the interface just prior to the eutectic solidification, and (4) the eutectic solidification. In contrast, (1) and (2) occurred nearly at the same time in the specimen containing 0.05 mass pct Mg. The addition of 0.05-mass pctMg significantly reduced the temperature range in which the graphite particles grew as the primary phase. Image-based analysis of melting behavior showed that even 0.05 mass pct addition was sufficient to modify the phase equilibrium of the liquid, γ-Fe, and graphite phases. Thus, the observed influence of Mg on the solidification sequence was attributed to the modification of the phase equilibrium. The influence was consistently explained by considering the shift of the eutectic composition to the carbon side in the pseudo-ternary system. It was also suggested that supersaturation of carbon in the melt increased as the temperature decreased even though the primary graphite particles existed. The supersaturation may cause the nucleation of the graphite particles just before the eutectic solidification.

I. INTRODUCTION

IT has been found that small addition of Ce or Mg to hypereutectic cast iron changed the morphology of graphite particles from a flake shape to a more compacted/spheroidal shape.[1,2] A number of studies have been done to investigate the mechanism of spheroidal graphite formation, to control the microstructure for commercial application.[3,4] In general, the formation of spheroidal graphite particles has been attributed to nucleation events and growth modes of graphite particles. This paper focuses on the influence of Mg additions, which are commonly used for producing spheroidal graphite particles, on solidification and melting behaviors of hypereutectic cast iron.

One important consideration in morphological transitions during solidification is nucleation. It has been proposed that both inclusions and bubbles act as nucleation sites. The bubbles in the melt can be produced by vaporization of Mg.[5–7] Sulfides and oxides are produced by the reaction of S/O with added Mg in the melt.[8–10] Silicates such as $MgO\text{-}SiO_2$ and $2MgO\text{-}SiO_2$ were also confirmed to be present in the ductile cast iron.[11] The chemical composition and crystal structure of the inclusions produced by adding ferrosilicon containing Mg were examined.[12] The observed inclusions were (Ca, Mg)—sulfides surrounded by (Mg, Al, Si, Ti)—oxides. A confocal scanning laser microscopy also observed the inclusions inside the spheroidal graphite particles.[13] The core of the MgS was surrounded by sulfides and oxides. It is obvious that the inclusions promote the graphite nucleation events. However, it is still not clear how the nucleation sites influence the morphology of the graphite particles.

Spheroidal graphite particles have been produced using the cast iron made from high-purity metals. The spheroidal graphite particles did not contain any impurity elements around the core region.[14] The results proved that the spheroidal shape was attributed to the nature of graphite growth. The role of added Mg is to remove some trace elements solved in solution in the melt, such as S and O. The influence of S concentration and cooling rate on the morphology of graphite particles were also investigated in the high-purity cast iron.[15] No spheroidal graphite particles were formed in the specimen with >0.008mass pctS at a cooling rate as high as 17 K/s. The spheroidal graphite particles were formed in the specimen with approximately 0.001mass pctS at 1.7 K/s. In the nearly S-free specimen (0.00015-mass pctS), the spheroidal graphite particles were easily

K. YAMANE, Researcher, is with the IHI Master Metal, Aioi, Hyogo 678-0041, Japan. H. YASUDA, Professor, and K. MORISHITA, Assistant Professor, are with the Department of Materials Science and Engineering, Kyoto University, Kyoto 606-0851, Japan. Contact e-mail: yasuda.hideyuki.6s@kyoto-u.ac.jp A. SUGIYAMA, Professor, is with the Department of Mechanical Engineering for Transportation, Osaka Sangyo University, Daito, Osaka 574-8530, Japan. T. NAGIRA, Assistant Professor, and M. YOSHIYA, Associate Professor, are with the Department of Adaptive Machine Systems, Osaka University, Suita, Osaka 565-0871, Japan. K. UESUGI, A. TAKEUCHI, and Y. SUZUKI, Researchers, are with the JASRI/SPring-8, Sayocho, Hyogo 679-5198, Japan.
Manuscript submitted September 22, 2014.
Article published online July 25, 2015

obtained even at 0.7 K/s. The results suggested that S and O solved in the melt could inhibit the intrinsic growth mode of graphite, and the role of Mg is to act like a scavenger.

It has been known that the solidification sequence in the cast iron was rather complicated.[16,17] For example, the morphology of the solidification structure including the graphite shape is significantly influenced by the solidification rate and the melt composition. The shape of graphite particles transforms from lamellar graphite in a coupled eutectic structure to compacted graphite, and from compacted graphite to spheroidal graphite in the divorced eutectic structure with increasing Mg or Ce content in the melt.[16–18] The results show that the divorced eutectic growth is normally selected in the melt which contains sufficient Mg or Ce, leading to spheroidal/compacted graphite particles in the matrix. In addition to the graphite morphology, the spheroidal graphite particles are surrounded by the quasi-spherical γ-Fe phase (austenite).[19]

The influence of Mg on the solidification sequence is still not understood quantitatively. Furthermore, the influence of Mg on the phase equilibrium between the liquid phase, the γ-Fe phase, and graphite has generally been almost neglected. It is of interest to examine the influence of Mg on the solidification sequence and the phase equilibrium. However, the direct experimental observation of the solidification sequence to confirm phase equilibrium in these alloys is challenging.

In recent years, radiography using synchrotron radiation X-rays has enabled to the observation of solidification in metallic alloys. In the early stages, solidification of Sn-, Al-, and Zn-based alloys were observed *in situ*.[20–29] The technique has been successfully applied to observe the evolution of solidification structures such as dendritic growth, the columnar/equiaxed transition, and dendrite arm fragmentation, and has been extended for observing the various phenomena related to solidification. For example, deformation of semisolid has been observed *in situ*.[30–32] The technique has also been developed for observing solidification of Fe-based alloys.[33,34] The developed technique was used to observe solidification of the cast iron with hypoeutectic composition (3.5C-2.6Si-0.3Mn-0.3Cu-0.7Ni in mass pct).[35] The dendrites of γ-Fe as the primary phase grew in advance, and the eutectic solidification followed behind the dendrites. In addition, some graphite particles grew in isolation, supporting a mode of divorced eutectic solidification.

Recently, solidification of hypereutectic cast iron (3.79C-3.1Si-0.14Mn-0.015S-0.04Mg in mass pct, CE = 4.8) was observed *in situ* by radiography.[36] The specimens were repeatedly melted and solidified. Since the Mg concentration decreased during melting due to vaporization of Mg (a fading effect), the influence of Mg was indirectly examined. In the initial run, the graphite particles with a spherical shape grew in the melt and were surrounded by γ-dendrites or the eutectic structure of γ-Fe and graphite. In the second and the third runs, the graphite particles with a spherical shape grew in the initial stage and then transformed from a spheroidal shape to a flake-like shape before being engulfed by the γ-dendrites and the eutectic structure. In

addition, the temperature range in which the graphite particles grew as the primary phase increased with decreasing Mg concentration.

In situ observation with a higher spacial resolution has also been done for hypereutectic cast iron specimens (CE = 4.59) with 0.002 Mg and 0.05 Mg.[37] EBSD analysis for the specimens after the observation showed that the spheroidal graphite particles had essentially the same crystallographic feature as those in the conventional cast iron.[38,39] It means that the growth of the graphite particles in the limited space (0.1 mm in thickness) was analogous to those in the ductile cast iron. In addition, Mg in solution in the melt decreased the temperature range in which the graphite particles grew as the primary phase. On the basis of the previous studies,[36,37] this paper firstly demonstrates the solidification sequence in the hypereutectic cast iron with and without Mg. Second, the influence of Mg on the phase equilibrium (liquid phase, γ-Fe and graphite) is presented. The influence was examined by an image-based analysis (referred to as differential image analysis). In the analysis, two different specimens put adjacent to one another in a specimen holder were heated together. Comparison of microstructure changes during the heating procedure gives the difference in phase transformation temperature. The role of Mg addition on the solidification sequence is discussed.

II. EXPERIMENTAL PROCEDURES

The chemical compositions of specimens are shown in Table I. Mg concentrations are 0.002mass pct and 0.05mass pct, respectively. In this paper, the former one is referred to as 0.002Mg and the later one 0.05Mg. The carbon equivalent value, which is calculated by [mass pctC] + [mass pctSi]/3, is 4.59 (hypereutectic compositions) for both specimens.

The observations of solidification were performed at the BL20XU beamline in SPring-8, Hyogo, Japan. The light source used was hybrid-type "in-vacuum" planar undulator. X-rays were monochromatized by the double crystal monochromator of Si (111), which was placed at 46 m from the source point. The experimental hatch was located at about 200 m from the light source. The observation of melting was performed at another beam line of BL20B2 in which the bending magnet is used as a light source. The X-ray energy used for the observations was 19 keV. Figure 1 shows a setup for the *in situ* observation. An ion chamber for measuring the intensity of the incident beam, a furnace with a graphite heater, a thin sample, and an X-ray imaging detector (consisting of a CMOS-type camera, an optical lens and a phosphor screen) were placed along the light axis. Details of the setup were described in a previous study.[34] The transmission image signals were converted into a digital format and stored with a format of 2000 × 1312 pixels and 16-bit resolution. The pixel size was 0.5 μm × 0.5 μm at BL20XU and 5 μm × 5 μm at BL20B2, respectively. The detector acquired, approximately, 1 frame per second. In the present setup, the spatial resolution was several μm at BL20XU and 10-20 μm at BL20B2, respectively.

Table I.   Initial Composition of 0.002Mg and 0.05Mg

Sample	C	Si	Mn	Mg	S	CE
0.05Mg	3.73	2.57	0.45	0.05	0.004	4.59
0.002Mg	3.69	2.71	0.45	0.002	0.004	4.59
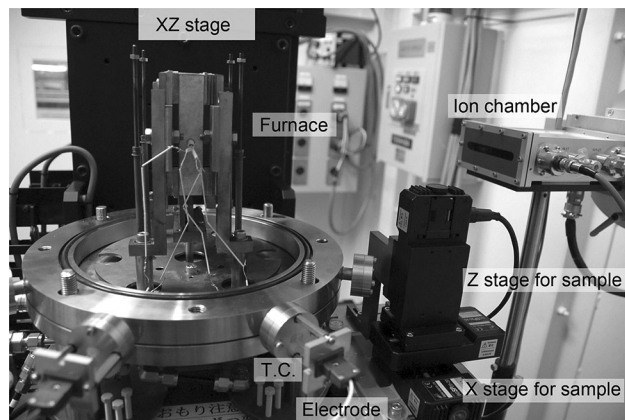
Fig. 1—Setup of the *in situ* observation for the Fe-based alloys.

Fig. 2—Typical solidification structure of hypereutectic cast iron after the *in situ* observations.[37] The specimen was melted several times.

Fig. 3—Configuration of two specimens in the specimen holder for the differential image analysis.

A specimen of 100 μm in thickness was inserted into a specimen holder, which consists of sapphire plates and BN plates. Melting and solidification were observed in under a vacuum (in the order of 10^{-3} torr). For the observation of solidification, the specimen was heated until the primary graphite particles were melted and then was cooled at a cooling rate of 0.17 K/s. This heating and cooling procedure was performed once for each specimen to avoid any fading. The transmission images were normalized by a transmission image of the liquid phase before the solidification started.

Figure 2 shows an example of the microstructure in a specimen with CE = 4.82 (3.79C-3.09Si-0.14Mn-0.015S-0.04Mg in mass pct) after several heating/cooling cycles.[34] Due to the evaporation of Mg from melt, spheroidal graphite, relatively small spheroidal/compacted graphite (referred to as E, explained in the next section), flake-like graphite, and eutectic graphite were observed. In the radiography, four different types of graphite appeared.

Differential image analysis was used to examine the influence of the Mg addition on the phase equilibrium. Two different specimens were inserted into a specimen holder and were separated by the Al_2O_3 plate to avoid contact of the melts. The configuration of the two specimens is shown in Figure 3. The dimensions of each specimen were approximately 2 mm in width, 5 mm in height, and 0.1 mm in thickness. The distance between the specimens was 1-2 mm in the horizontal direction. Since horizontal temperature gradient was sufficiently small at the observation area, temperature difference between the two specimens was less than 1K. The specimens were heated together at a heating rate of 0.194 K/s until both of the specimens were completely melted. Table II shows the comparison of the differential image analysis and the conventional differential thermal analysis. In the conventional differential thermal 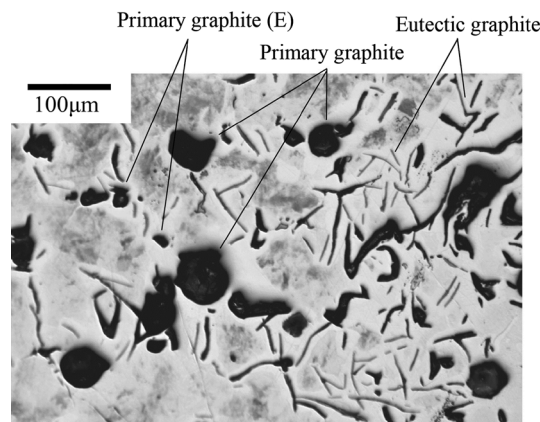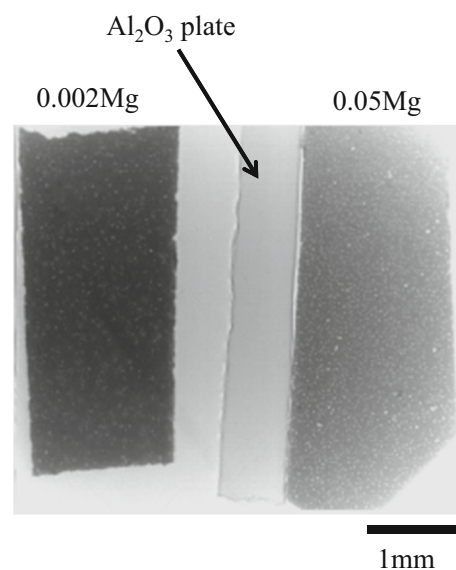analysis, either endothermic or exothermic heat in the specimen is detected. In the differential image analysis, microstructure change is directly detected by the radiography. Since the specimens (6 mg, 2 mm in width, 5 mm in height, 0.1 mm in thickness) have a relatively large surface area with respect to volume, the endothermic heat due to melting is easily transferred to outside the specimen. As a result, the resolution of temperature in the differential image analysis is relatively high, compared to that of the conventional DTA. However, the thermocouple in the furnace is not in physically contact with the specimen, and the heat

Table II. Comparison of the Differential Image Analysis Used in the Present Study and the Conventional DTA

	Differential Image Analysis By *In Situ* Observation	Conventional DTA
Measurement object	microstructure change	endothermic/exothermic heat
General versatility	very low	high
Mass of specimen	6 mg	100 mg
Shape of specimen	thin film (relatively high surface area)	droplet
Quantitative capability for enthalpy change	no	semi-qualitative
Accuracy of temperature	absolute: low relative: high	absolute value: high
Resolution of temperature	relatively high	relatively low due to temperature distribution
Sensitivity	depends on microstructure change	depends on heat release
Advantage	to detect microstructure change with relatively low enthalpy change	to detect phase transformation with sufficient enthalpy change

transfer is controlled by radiation in the measurement temperature range. Thus, the accuracy of specimen temperature in the radiographic experiments is much lower. The advantage of the differential image analysis is in the ability to detect relative difference in the melting temperature of the two specimens. In particular, the measurement of relative difference in liquidus temperature, where the remaining primary phase is completely melted, can be performed with a high degree of confidence because the radiography directly confirms the melting.

III. RESULTS AND DISCUSSION

A. *Nucleation and Growth of the Primary Graphite*

Figures 4(a) through (d) show the solidification structure in the 0.002 Mg specimen at a cooling rate of 0.17 K/s.[37] Graphite particles (indicated by the black arrows in (a)) were detected at $t = -124$ seconds. Most graphite particles seemed to be spheroidal (circular shape in 2D). It should be noted that the spheroidal shape is defined within the resolution capability, and it is possible the particles could exhibit a polyhedral shape due to the atomic bonding of the graphite. The transition to the flake-like shape was observed at $t > -99$ seconds. The γ-Fe dendrites immediately followed by the eutectic solidification of the γ-Fe and the graphite phases (referred to as the eutectic) are observed in Figure 4(d). Here, the eutectic structure exhibited a smoke-like contrast on the transmission images, since the eutectic graphite plates were overlapped each other on the transmission images. Surprisingly, a number of the graphite particles nucleated ahead of the eutectic front even though the primary graphite particles were pre-existing. In the 0.002 Mg sample, the graphite particles grew for 120 seconds and were engulfed by the γ-Fe dendrites and the eutectic solidification front.

As shown in Figure 4(d), the growth of the primary dendrite arms was not affected by the primary graphite particles. When the dendrite tip reached the graphite particles, the graphite particles were immediately surrounded by the γ phase (for example, the graphite particle that is on the left in the center) and then the primary arms developed again from the surrounding γ phase. Although the nucleation position of the γ phase was not able to be identified due to the limited observation area (1 mm × 0.65 mm), the wide area observation in the previous work[36] showed the γ phase nucleated in the vicinity of graphite particles. The observation suggested that the graphite particles could be a nucleation site for the γ phase.

Figure 4(i) shows the number of graphite particles in the observation area and the maximum length of a graphite particle.[37] Again, the temperature was defined to be zero when the eutectic solidification front reaches at the center of the observation area. As shown in Figure 2, the primary graphite particles were several 10 μm in diameter. Due to the large difference in X-ray absorption between graphite and the melt, the graphite particles with sizes larger than 5 μm were easily detected. Thus, it is capable of measuring the number with relatively high accuracy. All the nucleation events occurred within 3 K (−270 °C), and then, the growth rate of the graphite particle gradually decreased and became nearly zero in the temperature range from 10 K to 0 K (−263 °C to −273 °C). The temperature range in which the graphite particles grew independently was 20 K (−253 °C).

Different solidification structures were observed in the 0.05Mg specimen as shown in Figures 4(e) through (h).[37] Nucleation of graphite particles and dendrites of γ-Fe occurred nearly at the same time and they grew independently. Nucleation events of the primary graphite particles continuously occurred until the eutectic solidification commenced. The graphite particles with spherical shape grew for 20 seconds and then were engulfed by the eutectic front. In 0.05Mg, the temperature range in which the graphite particles grew independently was only 3 K to 4 K (−270 °C to −269 °C). As shown in Figure 4(i), the nucleation frequency of graphite particles in 0.05Mg was approximately three times larger than that in 0.002Mg. The continuous
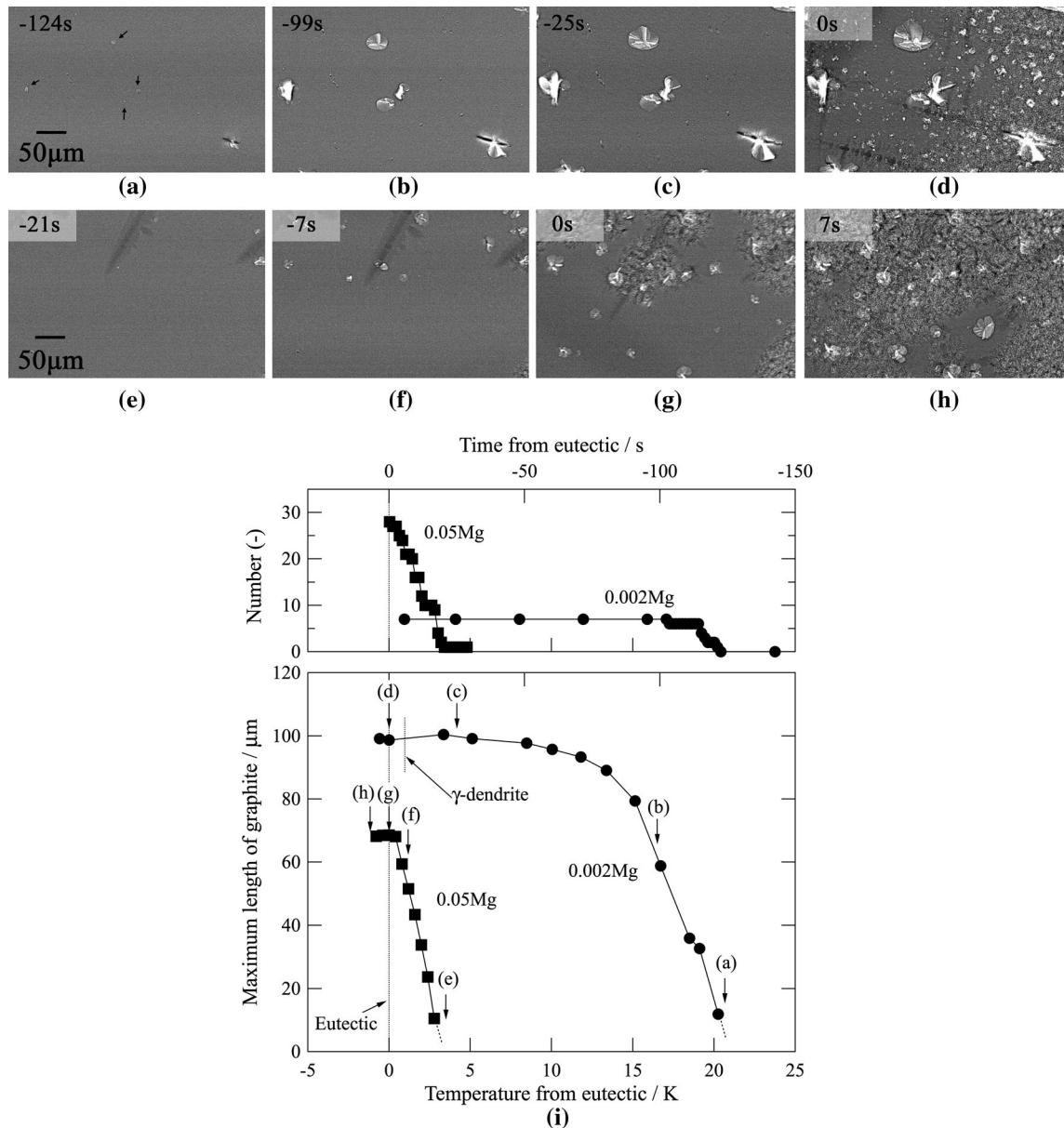
Fig. 4—(a) through (d) Solidification in 0.002Mg at 10K/s, (e) through (h) solidification in 0.05Mg at 10K/s, (i) number of graphite particles in the observation area and maximum length of graphite particles.[37] (a) through (h) in (i) correspond to the transmission images of (a) through (h). Time and temperature were designated zero when the eutectic solidification front reached the center of the observation area.

nucleation events and the increase in the nucleation frequency are likely to arise due to nucleation sites for graphite including sulfides and the oxides.[8–10] In addition, since no nucleation sites were detected on the transmission images, the inclusions acting as nucleation sites were less than the special resolution (several μm).

There are two possible explanations for the decrease in the temperature range in which the graphite particles grew independently. One is that the Mg addition modified the phase equilibrium (the thermodynamic influence). The other is that the addition of Mg inhibited nucleation of graphite, and consequently, the temperature range decreased (the kinetic influence). However, as the inhibition conflicts with the promotion of the

primary graphite nucleation as shown in Figure 4(i), it is important to consider the thermodynamic influence.

B. Solidification Sequence

The nucleation event of the graphite particles occurred just before the eutectic solidification started as shown in Figure 4. Since the graphite particles that nucleated in front of the eutectic interface are not clear in Figures 4(e) through (h), the close-up views of the transmission images around the primary graphite particles in the 0.002Mg and 0.05Mg specimens are shown in Figure 5. Graphite particles (white arrows) nucleated around the primary graphite particles just before the

eutectic solidification. Since the duration of growth for the graphite particles just before the eutectic solidification was short, the size was relatively small. In the metallographic observation as shown in Figure 2, the relatively small graphite particles (E) are observed. The observation indicates that two different primary graphite particles existed. The nucleation events just before the eutectic solidification suggested that carbon in the melt was supersaturated even though the primary graphite particles existed.

On the basis of the observations, the solidification sequences were identified for 0.002Mg and 0.05Mg.

For 0.002Mg,

L → Graphite

L → Graphite, L → γ-Fe　[divorced eutectic]

L → Graphite, L → γ-Fe, L → Graphite (E)
　　[divorced eutectic]

L → γ-Fe + Graphite [coupled eutectic]

For 0.05Mg,

L → Graphite or L → γ-Fe

L → Graphite, L → γ-Fe [divorced eutectic]

L → Graphite, L → γ-Fe, L → Graphite (E)
　　[divorced eutectic]

L → γ-Fe + Graphite [coupled eutectic]

In both specimens, the graphite particles and γ-Fe dendrites grew independently until the coupled eutectic solidification started. The coupled eutectic solidification was always initiated by the nucleation of Graphite (E).

C. Growth Kinetic of the Primary Graphite

Figures 6(a) through (c) show the primary graphite particles used for measurement of the maximum length, D. For example, "D" in Figure 6(b) is the length of a flake-like graphite plate in 0.002Mg. In 0.05Mg, the length was nearly equal to the diameter of the graphite particles as shown in Figure 6(c). Figure 6(d) shows the graphite length as a function of the local growth time (t_f). There is no clear difference between 0.002Mg and 0.05Mg at the initial stage ($t_f < 10$), where the graphite particles exhibited nearly spheroidal or compacted. The growth rate of the graphite particles in 0.002Mg gradually decreased at $t_f > 10$ seconds, and the length was proportional to $t_f^{1/4}$ at $t_f > 20$ seconds. When the dendritic growth of γ-Fe and the eutectic solidification stated at $t_f > 120$ seconds, the graphite particles rapidly grew and were engulfed by the eutectic solidification front. The rapid growth suggested that carbon atoms were supersaturated in the melt. Since the eutectic solidification was dominant at this stage as shown in Figure 5, the eutectic solidification front may reject carbon. The rejection could also result in graphite nucleation just prior to eutectic solidification.

Figure 7 shows a schematic illustration of a pseudo-binary phase diagram around the eutectic point. If the liquidus line is assumed to be linear, the amount of supersaturated carbon ΔC is proportional to the temperature drop from the liquidus temperature ΔT. This assumption should be valid because the temperature range of the primary graphite growth is only 20 K (-273 °C) in 0.002Mg and 3 K (-270 °C) in 0.05Mg. In the equilibrium condition, the amount of carbon to be consumed for the graphite growth is proportional to the local growth time at a constant cooling rate. For the
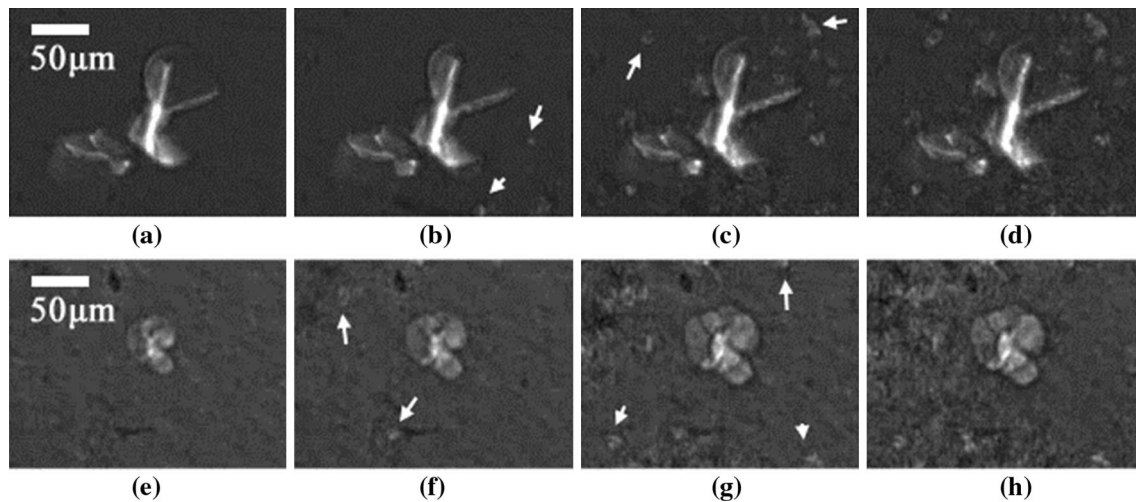

Fig. 5—Nucleation of graphite particles around the primary graphite particles just before the eutectic solidification. The white arrows indicate the graphite particles nucleated. The interval between frames is 2.36 s for (a) through (d) and 2.38 s for (e) through (h).
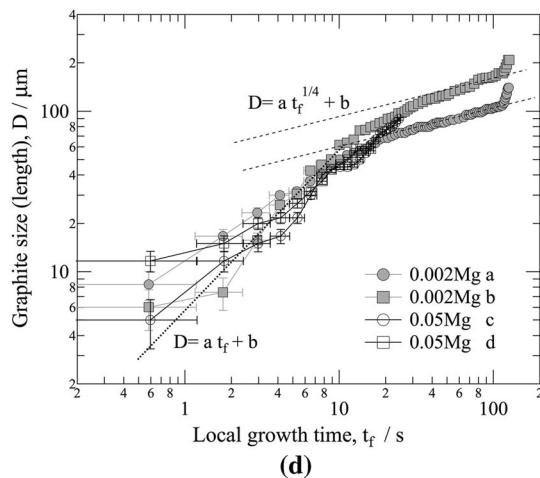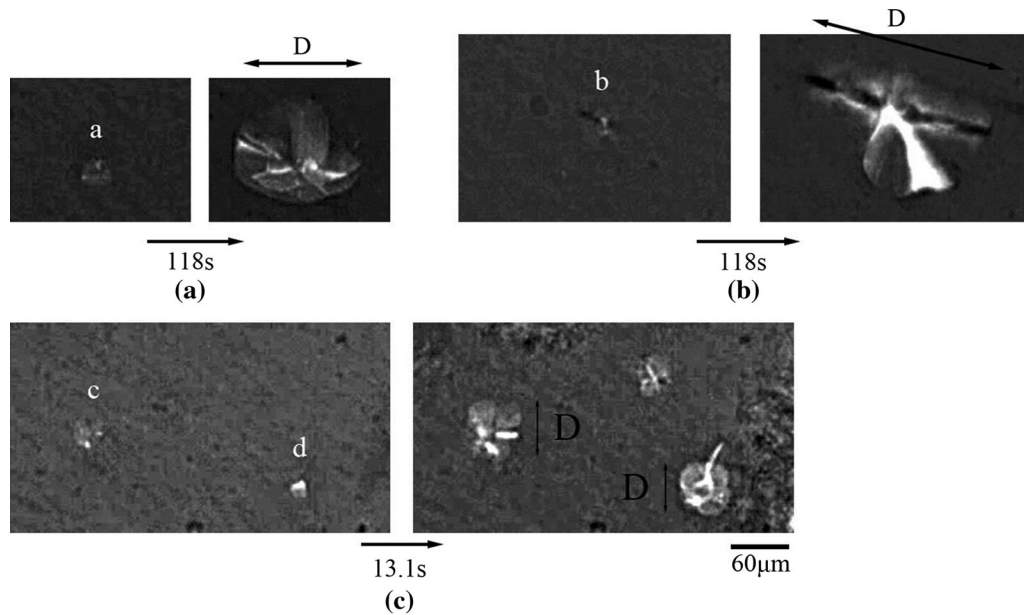
Fig. 6—(*a, b*) Close-up views of the graphite particles in 0.002Mg, (*c*) a close-up view of the graphite particles in 0.05Mg, (*d*) graphite size as a function of the local growth time. Notations a to d in (*d*) correspond to a to d in (*a*) through (*c*).

spherical growth, the relationship between the diameter, D, and the local growth time, t_f, is given by

$$D \propto t_f^n, \quad n = 1/3.$$

Carbon atoms are supersaturated in the melt, and supersaturated carbon atoms are consumed by graphite growth if n is larger than 1/3. On the other hand, $n < 1/3$ means that saturation of carbon atoms increases with decreasing temperature.

In the initial stage where the graphite particles were spheroidal in both specimens ($t_f < 10$ seconds), the value of n was nearly unity or slightly smaller. The graphite growth by accumulating supersaturated carbon atoms resulted in the higher value of n. In 0.05Mg, the value of n did not change remarkably until the engulfment by the eutectic solidification front. The value of n became 1/4 at the final stage in 0.002Mg. The lower value means that carbon supersaturating due to cooling was not fully consumed by the graphite growth, and the carbon

supersaturation increased as temperature decreased. The nucleation of the graphite particles just before the eutectic solidification is consistently explained.

D. *Differential Image Analysis*

Two possibilities were proposed to explain the influence of Mg on the temperature range in which the graphite particles grew independently. One is the thermodynamic influence and the other is the kinetic influence. To confirm which is dominant, the thermal image analysis was performed. Figure 8 shows the transmission images as a function of heating time. Since the heating rate was constant (0.194K/s), the heating time corresponds to a temperature [52 seconds is equal to 10 K (-263 °C)].

A part of the specimen was locally melted but the melting region was not extended at 10 seconds only in the 0.05Mg specimen. Mg atoms that were not consumed for the sulfides/oxides formation were rejected

into the melt from the solidification front. Microsegregation of Mg may result in the formation of Mg-containing compounds with a lower melting point. Melting of matrix at 60 seconds was immediately followed by melting of graphite particles in the 0.05Mg specimen. On the other hand, melting of the matrix started at 95 seconds, and melting of graphite was hardly observed until 165 seconds in the 0.002Mg specimen. 90 pct of observed graphite particles were melted at 150 seconds in the 0.05Mg specimen compared to 385 seconds in the 0.002Mg specimen.

The addition of 0.05mass pctMg slightly decreased the eutectic temperature [6 K (−267 °C)] and largely decreased the liquidus temperature [45 K (−228 °C)]. The difference between the liquidus and the eutectic
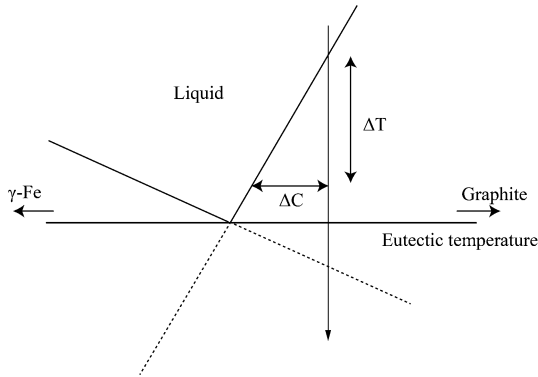
temperatures was estimated to be 56 K (−217 °C) for 0.002Mg and 17 K (−256 °C) for 0.05Mg, respectively. The temperature difference observed by the differential image analysis qualitatively agreed with the solidification sequences.

Conventional DTA was also done for the two specimens to compare with the differential image analysis. Figure 9 shows the conventional DTA curves of the 0.002Mg and the 0.05Mg specimens. Here, the temperature of matrix melting for 0.002Mg in the image analysis was assumed to the temperature "A" in the DTA curve. "B" is the melting of 90 pct graphite particles in 0.002Mg. "C" indicates the local melting in 0.05Mg, "D" the melting of the matrix, and "E" the melting of 90 pct graphite particle. The onset (D) of matrix melting in 0.05Mg was slightly lower than that (A) in 0.002Mg, and the width of the endothermic heat due to melting in 0.05Mg was narrower. The endothermic heat due to the local melting (C) was also detected in the DTA curve of 0.05Mg. In spite of the lower temperature resolution of the conventional DTA, the DTA curves qualitatively agreed with the results obtained by the differential image analysis. Therefore, the differential image analysis proved that the thermodynamic influence of the Mg addition largely reduced the difference between the liquidus and the eutectic temperatures.

E. Influence of Mg on Phase Equilibrium

Even the small amount of Mg modifies the phase equilibrium. The *in situ* observation and the differential

Fig. 7—Schematic illustration of pseudo-binary phase diagram of Fe-C around the eutectic point.
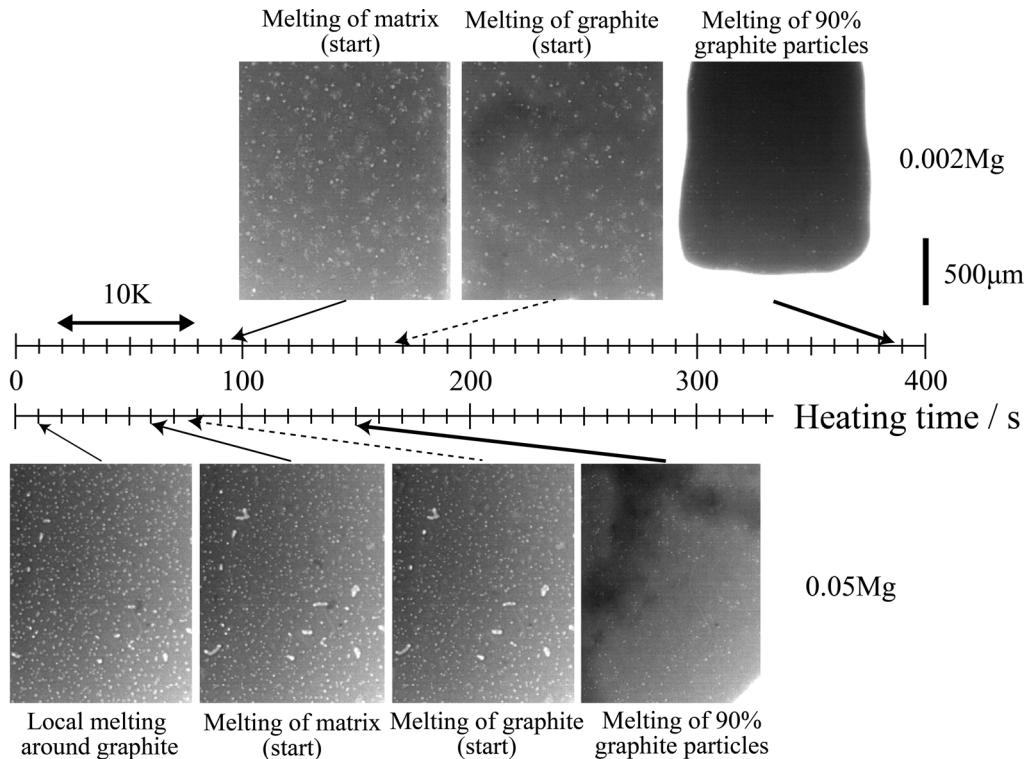

Fig. 8—Melting behavior in 0.002Mg and 0.05Mg during heating by the differential image analysis. The heating time is proportional to temperature (0.194K/s).
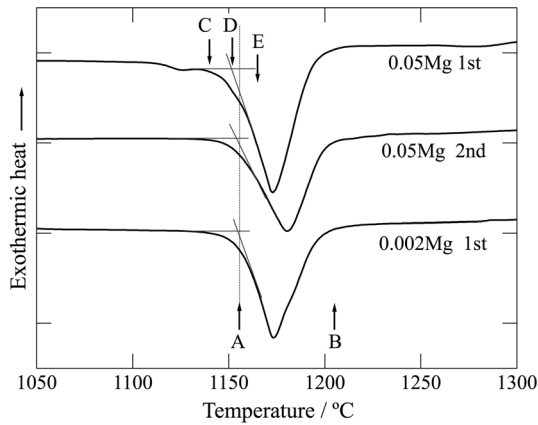
Fig. 9—DTA curves of the specimens containing 0.002 mass pctMg and 0.05 mass pctMg.
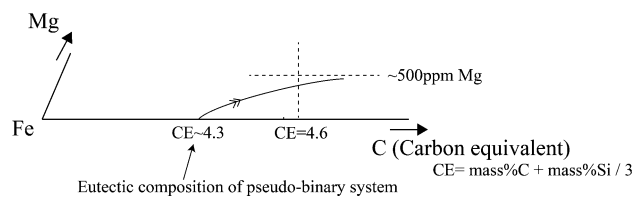

Fig. 10—Schematic illustration of isothermal section in Fe-C-Mg pseudo-ternary system around the Fe-C eutectic point.

image analysis showed that the composition (CE = 4.6) of the sample containing 0.05Mg approached the eutectic composition or a slightly hypereutectic composition.

Figure 10 shows a schematic illustration of an isothermal section in the pseudo-ternary phase diagram. If the eutectic composition shifts to the carbon side as Mg concentration increases, the influence of Mg addition can be consistently explained. Furthermore, the fact that the temperature difference between the liquidus and the eutectic temperatures decreased with the addition of Mg is also explained by the shift. A new carbon equivalent CE' can be virtually defined by

$$CE' = [\text{mass pctC}] + \frac{1}{3}[\text{mass pctSi}] - 6[\text{mass pctMg}]$$

The equation indicates that the contribution of Mg is 12 times larger than that of Si.

If the eutectic solidification follows the eutectic line as shown in Figure 10, carbon atoms are rejected into the melt from the eutectic solidification front. The shift of the eutectic line in the pseudo-ternary system gives a consistent explanation about the rapid growth and the graphite nucleation just before the eutectic solidification.

F. Contribution of the Thermodynamic Influence of Mg to Spheroidal Graphite

The influences of Mg on the solidification of the cast iron were (1) an increase of graphite nucleation events

and (2) a decrease of the temperature range in which the primary graphite particles grew independently. The graphite particles tended to be spheroidal in the initial stage of growth for 0.002Mg and 0.05Mg; however, a morphological change distinctly occurred in 0.002Mg. The shorter growth time or narrower growth temperature range due to the Mg addition is advantageous to keep the spheroidal shape. From this aspect, the influence of Mg addition could positively contribute to maintaining a spheroidal shape. However, it should be noted that this factor is a supplemental factor for the mechanism of spheroidal graphite formation. If a decrease in the temperature range was a dominant factor, the spheroidal graphite particles would be easily formed at slightly hypereutectic compositions even in the Fe-C binary system.

IV. SUMMARY

Time-resolved and *in situ* observations using synchrotron radiation X-rays were performed to examine the solidification and the melting behaviors in the hypereutectic cast iron specimens containing 0.002 and 0.05masspct Mg.

(1) The addition of 0.05mass pctMg significantly caused a significant increase of the graphite nucleation events and decreased the temperature range in which the primary graphite particles grew independently. The addition of 0.05mass pct Mg reduced the temperature range from 20 K to 3 K (−253 °C to −270 °C).

(2) The solidification sequences were identified in 0.002Mg and 0.05Mg containing specimens. In 0.002Mg specimens, the primary graphite particles were present and dendrites of γ-Fe also grew independently. Nucleation of graphite particles occurred again just before the eutectic solidification started. Solidification was completed with coupled eutectic growth. In 0.05Mg, the graphite particles and the γ-Fe phase nucleated and grew nearly at the same time. After the nucleation and growth, the sequence in 0.05Mg containing specimens was the same as that in 0.002Mg containing specimens.

(3) The growth of the graphite particles was examined using the relationship, $D \propto t_f^n$. In the initial stage, the value of n was nearly unity in 0.002Mg and 0.05Mg. The n became 1/4 at the final stage in 0.002Mg. The low value suggested that supersaturation of carbon in the melt increased as temperature decreased, even though the primary graphite particles existed.

(4) The differential image analysis demonstrated the influence of Mg on the phase equilibrium. The addition of 0.05mass pct Mg decreased the eutectic temperature slightly and the liquidus temperature remarkably. The solidification observed in the radiography was consistently explained by the thermodynamic influence.

(5) The observed influence of Mg addition is likely to be a supplemental factor in the mechanism of

spheroidal graphite formation, although the influence is not negligible for understanding the solidification of cast irons.

ACKNOWLEDGMENTS

ELECTRONIC SUPPLEMENTARY MATERIAL

REFERENCES

1. H. Morrogh and J.W. Grant: *J. Iron Steel Inst.*, 1947, vol. 155, p. 321.
2. A.P. Gagnebin, K.D. Millis, and N.B. Pilling: *Iron Age*, 1949, vol. 163, p. 77.
3. D. Stefanescu: *ASM Handbook: Casting*, ASM, Materials Park, 1988, vol. 15.
4. T. Skaland: *Proc. AFS Cast Iron Inoculation Conference*, Schaumburg, 2005, pp. 13–30.
5. H. Itofuji: *AFS Trans.*, 1996, vol. 104, pp. 79–87.
6. S. Yamamoto, Y. Kawano, Y. Murakami, B. Chang, and R. Ozaki: *Met. Sci.*, 1978, vol. 12, pp. 56–60.
7. M.J. Lalich and J.R. Hitchings: *AFS Trans.*, 1976, vol. 84, pp. 652–58.
8. K.M. Muzumdar and J.F. Wallace: *AFS Trans.*, 1972, vol. 80, pp. 317–28.
9. K.M. Muzumdar and J.F. Wallace: *AFS Trans.*, 1973, vol. 81, pp. 412–23.
10. G.X. Sun and C.R. Loper: *AFS Trans.*, 1983, vol. 91, pp. 639–46.
11. T. Askaland: *Metall. Trans. A.*, 1993, vol. 24A, pp. 2321–45.
12. M.H. Jacobs, T.J. Law, D.A. Melford, and M.J. Stowell: *Met. Technol.*, 1974, vol. 1, pp. 490–500.
13. N. Klorca-Isern, J. Tartera, M. Espanol, M. Marsal, G. Bertran, and S. Castel: *Micron*, 2002, vol. 33, pp. 357–64.
14. B. Dhindaw and J.D. Verhoeven: *Metall. Trans. A*, 1980, vol. 11A, pp. 1049–57.
15. H. Nakae, S. Jung, H. Inoue, and H. Shin: *Proc. 66th World Foundry Congress*, Istanbul, 2004, pp. 917–928.
16. D.M. Stefanescu: *Metall. Mater. Trans. A*, 2007, vol. 38A, pp. 1433–47.
17. H. Zhao, M. Zhu, and D.M. Stefanescu: *Key Eng. Mater.*, 2011, vol. 457, pp. 324–29.
18. Y.X. Li, B.C. Liu, and C.R. Loper, Jr: *AFS Trans.*, 1990, vol. 98, pp. 483–88.
19. G. Rivera, R. Boeri, and J. Sikora: *J. Adv. Mater. Res.*, 1997, vols. 4–5, p. 169.
20. R.H. Mathiesen, L. Arnberg, F. Mo, T. Weitkamp, and A. Snigirev: *Phys. Rev. Lett.*, 1999, vol. 83, pp. 5062–65.
21. R.H. Mathiesen, L. Arnberg, K. Ramsoskar, T. Weitkamp, C. Rau, and A. Snigirev: *Metall. Mater. Trans. B*, 2002, vol. 33B, pp. 613–23.
22. N. Mangelinck-Noel, H. Nguyen-Thi, G. Reinhart, T. Schenk, V. Cristiglio, M.D. Dupouy, J. Gastaldi, B. Billia, and J. Hartwig: *J. Phys. D*, 2005, vol. 38, pp. A28–32.
23. B. Li, H.D. Brody, D.R. Black, H.E. Burdette, and C. Rau: *J. Phys. D*, 2006, vol. 39, pp. 4450–56.
24. L. Arnberg and R.H. Mathiesen: *JOM*, 2007, vol. 59, pp. 20–26.
25. D. Ruvalcaba, R.H. Mathiesen, D.G. Eskin, L. Arnberg, and L. Katgerman: *Acta Mater.*, 2007, vol. 55, pp. 4287–92.
26. H. Yasuda, T. Nagira, H. Harada, T. Sawai, H. Sindoh, and K. Nishimura: *Proc. 7th Int. Conf. Zinc and Zinc Alloy Coated Steel Sheet*, Suita, 2007, pp. 545–49.
27. G. Reinhart, A. Buffet, H. Nguyen-Thi, B. Billia, H. Jung, N. Mangelinck-Noel, N. Bergeon, T. Schenk, J. Hartwig, and J. Baruchel: *Metall. Mater. Trans. A*, 2008, vol. 39A, pp. 865–74.
28. H. Yasuda, Y. Yamamoto, N. Nakatsuka, T. Nagira, M. Yoshiya, A. Sugiyama, I. Ohnaka, K. Umetani, and K. Uesugi: *Int. J. Cast Met. Res.*, 2009, vol. 21, pp. 125–28.
29. T.M. Wang, J.J. Xu, T.Q. Xiao, H.L. Xie, J. Li, T.J. Li, and Z.Q. Cao: *Phys. Rev. E*, 2010, vol. 81, p. 042601.
30. C.M. Gourlay, A.K. Dahle, T. Nagira, N. Nakatsuka, K. Nogita, K. Uesugi, and H. Yasuda: *Acta Mater.*, 2011, vol. 59, pp. 4933–43.
31. T. Nagira, C.M. Gourlay, A. Sugiyama, M. Uesugi, Y. Kanazawa, M. Yoshiya, K. Uesugi, K. Umetani, and H. Yasuda: *Scr. Mater.*, 2011, vol. 64, pp. 1129–32.
32. T. Nagira, S. Morita, H. Yokota, H. Yasuda, C.M. Gourlay, M. Yoshitya, A. Sugiyama, K. Uesugi, Y. Takeuchi, and Y. Suzuk: *Metall. Mater. Trans. A*, 2014, vol. 45A, pp. 1415–24.
33. H. Yasuda, Y. Yamamoto, N. Nakatsuka, T. Nagira, M. Yoshiya, A. Sugiyama, I. Ohnaka, K. Umetani, and K. Uesug: *Int. J. Cast Met. Res.*, 2008, vol. 22, pp. 15–21.
34. H. Yasuda, T. Nagira, M. Yoshiya, N. Nakatsuka, A. Sugiyama, K. Uesugi, and K. Umetani: *ISIJ Int.*, 2011, vol. 51, pp. 402–08.
35. A. Sugiyama, H. Yasuda, T. Nagira, M. Yoshiya, K. Uesugi, K. Umetani, and I. Ohnaka: *J. Jpn. Found. Eng. Soc.*, 2011, vol. 82, pp. 131–36.
36. K. Yamane, H. Yasuda, A. Sugiyama, T. Nagira, M. Yoshiya, K. Uesugi, K. Umetani, C. Ushigome, and A. Sato: *J. Jpn. Found. Eng. Soc.*, 2013, vol. 85, pp. 760–70.
37. K. Yamane, A. Sugiyama, T. Nagira, M. Yoshiya, H. Yasuda, Y. Tanaka, A. Sato, K. Uesugi, A. Takeuchi, Y. Suzuki, H. Honda, and K. Sato: *J. Jpn. Found. Eng. Soc.*, 2014, vol. 86, pp. 461–70.
38. D. Holmgren, R. Kallbom, and I.L. Svensson: *Metall. Mater. Trans. A*, 2007, vol. 38A, pp. 268–75.
39. T. Hara, T. Maekawa, T. Kawabata, K. Terayama, S. Ikeno, and K. Matsuda: *Arch. Metall. Mater.*, 2013, vol. 58, pp. 431–32.